Nano-Micro Lett. (2018) 10:62
https://doi.org/10.1007/s40820-018-0215-3

ARTICLE

MoS_2 Nanosheet Arrays Rooted on Hollow rGO Spheres as Bifunctional Hydrogen Evolution Catalyst and Supercapacitor Electrode

Shizheng Zheng[1] · Lijun Zheng[1] · Zhengyou Zhu[1] · Jian Chen[1] · Jianli Kang[2] · Zhulin Huang[3] · Dachi Yang[1]

Received: 20 April 2018 / Accepted: 18 June 2018 / Published online: 9 July 2018
© The Author(s) 2018

Highlights

- MoS_2 nanosheets arrays were vertically rooted on hollow rGO spheres (h-rGO@MoS_2) via an optimized dual-template strategy.
- The bifunctional h-rGO@MoS_2 architecture exhibit enhanced hydrogen evolution reaction performance (105 mV, onset potential) and higher specific capacitance (238 F g^{-1} at 0.5 A g^{-1}) as a supercapacitor electrode than pristine MoS_2.

Abstract MoS_2 has attracted attention as a promising hydrogen evolution reaction (HER) catalyst and a supercapacitor electrode material. However, its catalytic activity and capacitive performance are still hindered by its aggregation and poor intrinsic conductivity. Here, hollow rGO sphere-supported ultrathin MoS_2 nanosheet arrays (h-rGO@MoS_2) are constructed via a dual-template approach and employed as bifunctional HER catalyst and supercapacitor electrode material. Because of the expanded interlayer spacing in MoS_2 nanosheets and more exposed electroactive S–Mo–S edges, the constructed h-rGO@MoS_2 architectures exhibit enhanced HER performance. Furthermore, benefiting from the synergistic effect of the improved conductivity and boosted specific surface areas (144.9 m^2 g^{-1}, ca. 4.6-times that of pristine MoS_2), the h-rGO@MoS_2 architecture shows a high

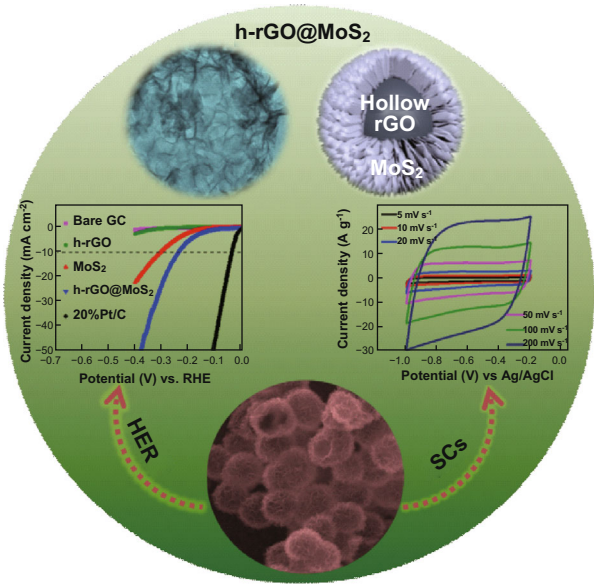

Electronic supplementary material The online version of this article (https://doi.org/10.1007/s40820-018-0215-3) contains supplementary material, which is available to authorized users.

✉ Dachi Yang
yangdachi@nankai.edu.cn

[1] Key Laboratory of Photoelectronic Thin Film Devices and Technology of Tianjin, Department of Electronics, College of Electronic Information and Optical Engineering, Nankai University, Tianjin 300350, People's Republic of China

[2] School of Material Science and Engineering, Tianjin Polytechnic University, Tianjin 300387, People's Republic of China

[3] Key Laboratory of Materials Physics, and Anhui Key Laboratory of Nanomaterials and Nanotechnology, Institute of Solid State Physics, Chinese Academy of Sciences, Hefei 230031, People's Republic of China

specific capacitance (238 F g^{-1} at a current density of 0.5 A g^{-1}), excellent rate capacitance, and remarkable cycle stability. Our synthesis method may be extended to construct other vertically aligned hollow architectures, which may serve both as efficient HER catalysts and supercapacitor electrodes.

Keywords MoS_2 · Reduced graphene oxide (rGO) · Hollow spheres · Hydrogen evolution reaction (HER) · Supercapacitor

1 Introduction

The worsening energy crisis and environmental pollution have stimulated increased research into exploiting sustainable, renewable energy sources, and advanced energy-storage devices. Hydrogen, a clean energy source with the highest gravimetric energy density (143 kJ g^{-1}) [1], is considered as a promising alternative to fossil fuels and has, thus, attracted significant attention. Water electrolysis is a simple way to produce highly pure hydrogen; but the best-performed Pt-based electrocatalysts suffer from their high cost and scarcity of platinum [2, 3]. Additionally, due to the low cost, rapid charge–discharge process, and long cycling stability, supercapacitors have emerged as promising energy-storage devices to meet the burgeoning demand [4, 5]. Nevertheless, the energy density of supercapacitors is still less than satisfactory [6].

To address this bottleneck, emerging 2D materials, particularly MoS_2, have been widely studied as hydrogen evolution reaction (HER) catalysts [7–14] and supercapacitor electrode materials [15, 16]. Unfortunately, because of the poor intrinsic conductivity and easy aggregation, the HER catalytic activity and supercapacitive performance of bulk MoS_2 are poor [17, 18]. Accordingly, significant efforts have been devoted to confine the growth of MoS_2 using conductive matrix as template [19, 20]. Reduced graphene oxide (rGO), a layered carbon material with large-specific surface area and excellent electrical conductivity, has been proven to be an effective matrix that can endow MoS_2 with specific shapes, expand the interlayer spacing, and increase the conductivity [17, 21–26]. For example, Dai and coworkers synthesized a MoS_2/rGO hybrid structure via a solvothermal process, and the product benefitted from the synergistic effect of strong chemical and electronic coupling effects, an abundance of electroactive edges, and improved conductivity; thus, the hybrid exhibited enhanced HER performance [17]. Although remarkable progress has been achieved toward improving the HER performance by introducing graphene oxide as a growth matrix, the performance is still far from satisfactory. On the one hand, the inevitable restacking of graphene oxide, arising from the strong sheet-to-sheet π–π interactions [27], hampers the full use of the active surfaces. On the other hand, the limited ion diffusion and mass transport of the flat structure lead to the unsatisfactory HER catalytic activity.

Construction of hierarchical hollow architectures is deemed to be an effective strategy to enhance the electrochemical properties because of the advantages of a high surface-to-volume ratio and open structure [28–30]. In addition, the cavities in the hollow structures can serve as "ion-buffering reservoirs" to shorten the ion transport distances [31]. Previous papers [32, 33] have reported the application of conductive carbon shells as supports, yielding hierarchical hollow architectures; however, the lack of functional groups on surface constrains the growth of MoS_2 to ultrathin nanosheets. Moreover, the relatively thick carbon shells (> 20 nm) have adverse effect on ion diffusion and mass transport. Based on the above considerations, a facile SiO_2-template-based method is designed to fabricate hollow graphene spheres as supports to confine the growth of MoS_2 nanosheet arrays. It is anticipated that the restacking of GO would be prevented by SiO_2 templates, and MoS_2 is expected to be vertically supported on the GO shells. This expected hollow architecture possesses advantages of enhanced surface area, as well as more exposed electroactive sites, and, thus, is expected to exhibit enhanced HER catalytic activity and supercapacitive performance [34]. However, there have been only few reports on the use of hollow rGO spheres as a matrix to construct hierarchical architectures that serve both as HER catalysts and supercapacitor electrode materials.

In this study, 3D rGO hollow sphere-supported ultrathin MoS_2 nanosheets were prepared, as illustrated in Scheme 1. First, GO was intimately coated around positively charged SiO_2 spheres by electrostatic incorporation. Subsequently, ultrathin MoS_2 nanosheets were vertically grown around the GO shells via a hydrothermal process. Finally, the SiO_2 cores were fully removed by chemical etching. In such 3D architectures, the vertically aligned MoS_2 nanosheets with a large number of electroactive S–Mo–S edges and expanded (002) interlayer spacings were observed to be tightly anchored on the graphene surface. Benefitting from the expanded (002) interlayer spacing and the exposed electroactive S–Mo–S edges, the h-rGO@MoS_2 structure exhibited efficient HER catalytic activity with an overpotential of ca. 230 mV at 10 mA cm^{-2}. In addition, because of the boosted specific surface area and conductivity, remarkable supercapacitive

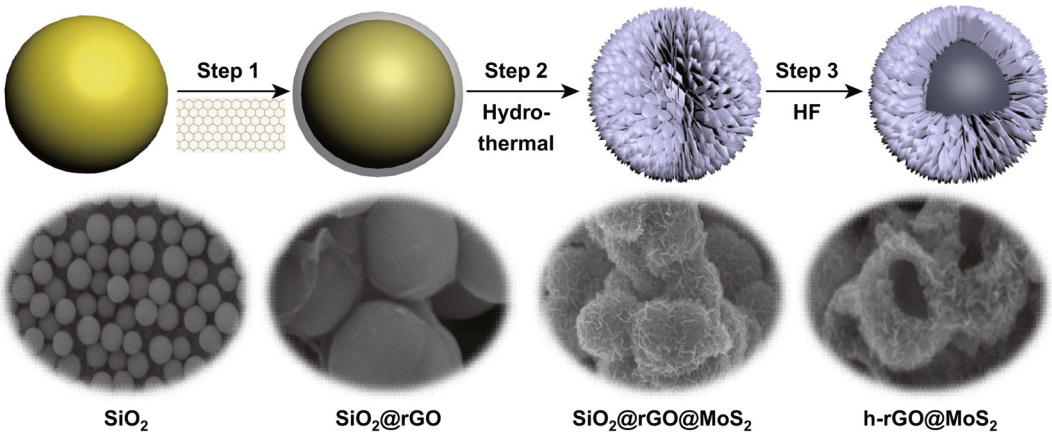

Scheme 1 Schematic illustration of the synthetic process of h-rGO@MoS_2

performance with high specific capacitance (238 F g^{-1} at 0.5 A g^{-1}) was achieved.

2 Experimental Section

2.1 Synthesis of the h-rGO@MoS_2 Architecture

First, GO sheets and SiO_2 spheres were prepared via a modified Hummers' method [35] and typical Stöber method [36], respectively. Before the GO wrapping process, SiO_2 spheres were decorated with (3-aminopropyl) triethoxysilane (APTES) [37] to obtain a positively charged surface. Second, during the GO coating process, 0.5 g of positively charged SiO_2 was dispersed in 300 mL of DI-water in a supersonic bath, and, then, 50 mL of 0.1 mg L^{-1} GO was dropped into the solution with continuous stirring. Subsequently, the SiO_2@GO powders were obtained after filtration and drying in an oven at 60 °C, followed by grinding. Next, 0.5 g of the as-synthesized SiO_2@GO powder was re-dispersed in 35 mL DI-water, followed by the addition of 0.3 g of $Na_2MoO_4{\cdot}2H_2O$ and 0.8 g of thiourea to the solution. Subsequently, 1 mL concentrated HCl (36 wt%) was added to adjust the pH value. After 1 h stirring, the blue mixture was transferred to a 50-mL Teflon-lined stainless-steel autoclave and kept at 200 °C for 24 h. After that, the black SiO_2@-rGO@MoS_2 sample was washed thoroughly and dried at 60 °C, followed by vacuum calcination at 350 °C for 2 h. Finally, the SiO_2 templates were removed via etching in 10% HF while stirring for 12 h, and h-rGO@MoS_2 hollow spheres were obtained. For comparison, SiO_2/MoS_2 and pristine MoS_2 were synthesized under the same conditions without the addition of GO and SiO_2@rGO template. Additionally, hollow rGO(h-rGO) spheres were synthesized via GO coating, hydrothermal reduction, and a SiO_2 etching process.

2.2 Characterization

The as-prepared samples were characterized by X-ray diffraction (XRD) using a Cu Kα radiation source (λ = 1.5406 Å) operating at 40 kV and 100 mA. Field-emission scanning electron microscopy (FE-SEM, JEOL-6701F), transmission electron microscopy (TEM, JEOL-2010), and high-resolution TEM (HRTEM, JEOL-2010) measurements were also carried out. X-ray photoelectron spectroscopy (XPS) measurements were carried out using a Thermo Scientific ESCALAB 250Xi instrument. The specific surface areas were analyzed using a Bei Shi De (3H-2000PM2) instrument and calculated using the Brunauer–Emmett–Teller (BET) model. The Raman spectra were recorded using an RTS-HiR-AM with excitation at 532 nm and a power of 5 μW.

2.3 Electrochemical Evaluations

For HER evaluation, the electrochemical tests were carried out in a three-electrode system with 0.5 M H_2SO_4 as the electrolyte and a Ag/AgCl electrode and graphite rod as the reference and counter electrodes, respectively. For these experiments, 10 mg pristine MoS_2 and 10 mg h-rGO@MoS_2 were dispersed in 1 mL liquor (0.75 mL water + 0.15 mL alcohol + 0.1 mL 5 wt% Nafion) and sonicated for 2 h. Then, 8 μL liquor was dropped onto the glassy carbon (GC) electrode using a microsyringe and dried at room temperature, and the mass loading of catalyst was calculated to be 400 μg cm^{-2}. The electrolytes were bubbled with N_2 before measurement and flowed over the electrolyte during the scanning process to exclude O_2. The measured potentials were referenced to the reversible

hydrogen electrode (RHE) by adding a value of (0.197 + 0.059 pH) V. All data are presented without *i*R compensation.

For the evaluation of the supercapacitor, the working electrodes were prepared similarly to previous methods [38]. First, as-prepared samples (MoS_2 and h-rGO@MoS_2), carbon black, and polyvinylidene difluoride (PVDF) were mixed in mass ratio of 8:1:1 and ground to slurry by adding *N*-methyl pyrrolidone (NMP). Second, the obtained slurry was then painted onto carbon cloth current collectors, yielding a calculated active area of 1 cm^2. Finally, the resultant working electrodes were dried at 60 °C for 24 h and pressed at 10 MPa. All electrochemical experiments were performed in 1 M Na_2SO_4 solution with platinum foils as the counter electrode and Ag/AgCl as the reference electrode, respectively. An electrochemical work station (CH Instruments, CHI760e) was employed for the cyclic voltammetry (CV), electrochemical impedance spectroscopy (EIS) measurements, and galvanostatic charge–discharge (GCD) tests. The EIS measurements were recorded with an AC voltage amplitude of 5 mV and a frequency range from 100 kHz to 0.01 Hz. Galvanostatic charge–discharge investigations were carried out from -1 to -0.2 V at current densities of 0.5, 1, 2, 3, 4, and 6 A g^{-1}.

3 Results and Discussion

To verify the morphologies of the SiO_2, SiO_2@GO, and h-rGO@MoS_2 architecture, SEM and TEM were used. Figure 1a shows an SEM image of the SiO_2 template prepared via the Stöber method, in which the SiO_2 particles are uniform spheres with diameters of ca. 350 nm. After decoration with APTES and coating with GO, the glossy surface of SiO_2 was wholly wrapped with GO, the thickness of which is less than 10 nm (Fig. 1b). Accordingly, because of the template effect of the SiO_2 spheres, the aggregation of GO sheets was hindered, and the available surface area for MoS_2 growth was increased. As shown in Fig. 1c, the thin MoS_2 nanosheets are vertically rooted on SiO_2@GO surface, forming a unique 3D hierarchical architectures. This arises from the abundant hydrophilic functional groups anchored on the surface of GO, that can attract and adsorb MoO_4^{2-} [39], resulting in the formation of well-dispersed MoS_2 nanosheets during the hydrothermal process. Notably, none of scattered MoS_2 nanosheets can be seen in the SEM image, revealing the appropriate addition of Mo precursors. As a comparison, SiO_2 spheres without a GO layer were used directly as the growth template, and no MoS_2 nanosheets were found at the roots (Fig. S1), which can be ascribed to the lack of anchoring nucleation sites for MoO_4^{2-} on the SiO_2 surface. Moreover, because of the stacking nature, pristine MoS_2 sheets synthesized without SiO_2@GO templates tended to tangle and aggregate, finally forming stacked "solid flowers" (Fig. S2). Therefore, the GO in this work serves as a template to confine the growth of the MoS_2 nanosheets and inhibit aggregation. To achieve a hollow architecture, HF was used as the etching agent to remove the SiO_2 template, and the final h-rGO@MoS_2 spheres are shown in Fig. 1d. As expected, h-rGO@MoS_2 retains its initial 3D architecture with a diameter of about 480 nm. Due to the 3D architecture, h-rGO@MoS_2 has a large surface area and more exposed S–Mo–S electroactive edges, which was

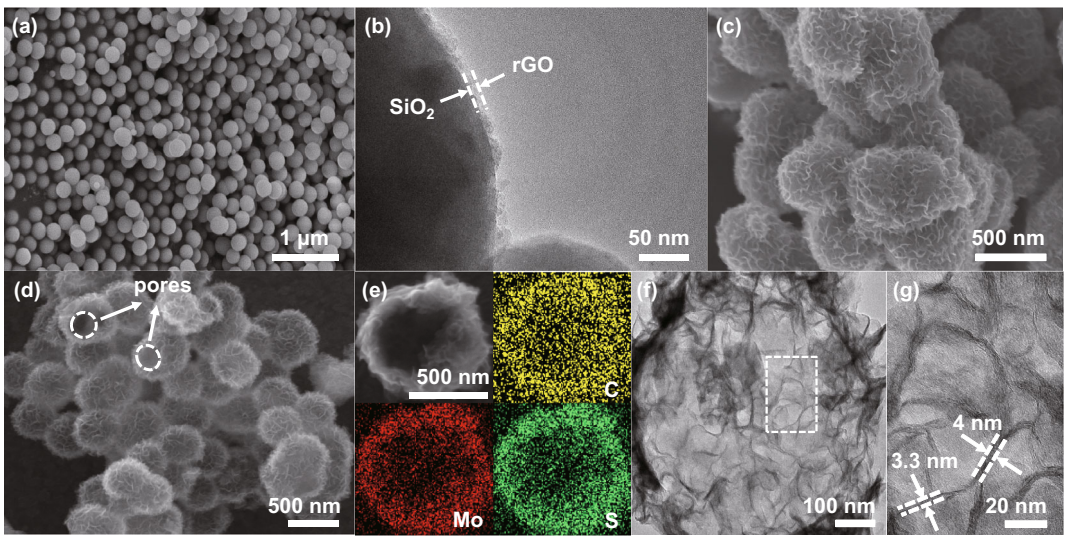

Fig. 1 The SEM and TEM images of **a** the SiO_2 sphere templates, **b** SiO_2@GO, and **c** SiO_2@GO@MoS_2. **d** SEM images of the h-rGO@MoS_2 spheres. **e** EDS elemental mapping results of the h-rGO@MoS_2 spheres. C arises from rGO, Mo and S arises from MoS_2. **f** TEM image of h-rGO@MoS_2, and **g** the HRTEM image of the white area in **f** showing several sheets of MoS_2

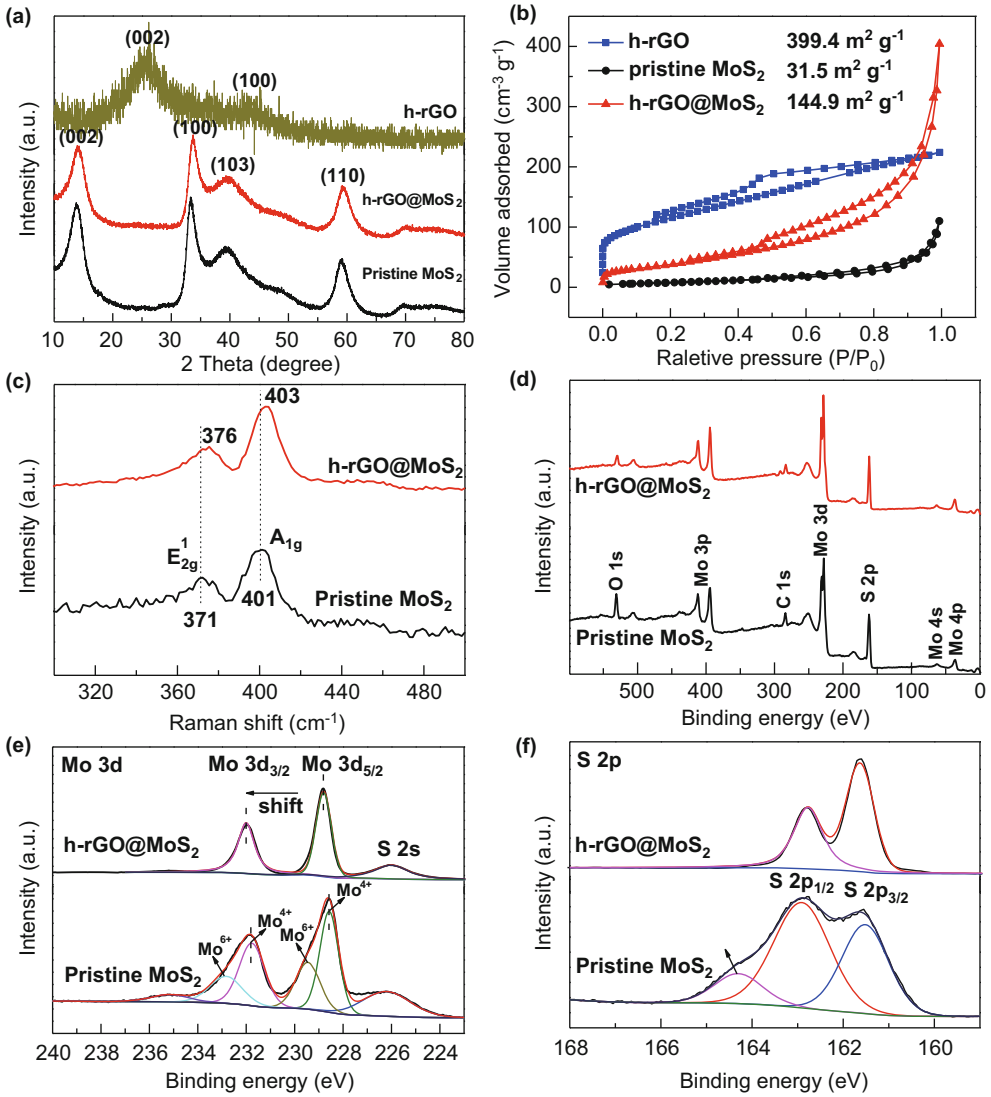

Fig. 2 **a** XRD spectra of h-rGO, pristine MoS_2, and h-rGO@MoS_2. **b** N_2 adsorption–desorption curves of h-rGO, pristine MoS_2, and h-rGO@MoS_2. The corresponding specific surface areas are given in the top left corner. **c** Raman spectra of pristine MoS_2 and h-rGO@MoS_2 measured with 532 nm excitation. **d** Survey spectra of pristine MoS_2 and h-rGO@MoS_2. **e**, **f** The high-resolution Mo 3d and S 2p XPS spectra of pristine MoS_2 and h-rGO@MoS_2

confirmed by N_2 adsorption–desorption experiments (Fig. 2b).

To reveal the elemental distribution, energy-dispersive X-ray spectroscopy (EDS) analysis of the h-rGO@MoS_2 was conducted, as shown in Fig. 1e. As shown, a hollow sphere with a cavity is observed, confirming the formation of a hollow architecture. Moreover, elemental C is well spatially distributed at the core, whereas Mo and S are scattered on the outer surface of the shells, indicating that MoS_2 is well dispersed on the surface of rGO. To obtain further information about the h-rGO@MoS_2 architecture, TEM observation was conducted, as shown in Fig. 1f. As clearly shown in the image, 3D hierarchical hollow spheres with cavities were formed, further revealing the successful formation of hollow architecture. Notably, the existence of these cavities can work as "ion-buffering reservoirs" to reduce the diffusion distance of electrolyte ions [31]. To ensure the layer structure of h-rGO@MoS_2, corresponding HRTEM measurements are performed in Fig. 1g. As can be seen, the vertically aligned MoS_2 nanosheets have thicknesses of about 3.3–4 nm (5–6 layers), thinner than that of pristine MoS_2 (Fig. S2). Moreover, the interlayer spacing of the MoS_2 nanosheets was measured to be ca. 0.65 nm (Fig. S3), which is assigned to the expanded (002) interlayer spacing of hexagonal MoS_2 [40] and agrees well with the results of XRD analysis (Fig. S4). The expanded interlayer spacing can increase the diffusion kinetics of ions and the interlayer conductivity [41] and, thus, could

enhance the HER performance. As a result, 3D hollow rGO spheres confine the growth of MoS_2 to form highly dispersed and vertically aligned ultrathin nanosheets with large surface area, exposed S–Mo–S electroactive edges, and expanded (002) interlayer spacing, which promise remarkable HER catalytic performance and supercapacitance.

The crystallographic structures (Fig. 2a) of h-rGO, pristine MoS_2, and h-rGO@MoS_2 architecture were identified via XRD characterization. In the XRD analysis of rGO, two broad peaks appear at $2\theta = 25°$ and 43°, demonstrating that graphene oxide was reduced to rGO. With respect to the XRD spectra of MoS_2 and h-rGO@MoS_2, both patterns contain peaks corresponding to semi-conductive hexagonal crystalline (2H) MoS_2, confirming that no impurity phases were introduced via the SiO_2 template method. It is worth noting that the (002) diffraction peak in Fig. S4 is shifted from 14.1° (MoS_2) to 13.7° in h-rGO@MoS_2, further revealing the expansion of (002) interlayer spacing. The broad diffraction peak corresponding to amorphous SiO_2 (located at $2\theta = 22.5°$, Fig. S5) was not detected, confirming that the SiO_2 templates had been successfully removed. In addition, no diffraction peaks of rGO were present on account of its low weight ratio.

The specific surface area is a key factor that has a significant influence on the HER catalytic performance and specific capacitance. To evaluate the specific surface area, N_2 adsorption–desorption characterization was carried out for h-rGO, pristine MoS_2, and the h-rGO@MoS_2 architecture, and the results are shown in Fig. 2b. All the curves present type-IV hysteresis loops (IUPAC classification), which may be closely related to the flower-like MoS_2 or 3D hollow rGO and h-rGO@MoS_2 architectures, in accordance with the SEM observations. Because of the hollow structure and unstacked layers, h-rGO spheres exhibit the highest specific surface area of about 399.4 $m^2\ g^{-1}$. Moreover, after the MoS_2 nanosheets had vertically grown on the surface of h-rGO, the BET surface area of the h-rGO@MoS_2 architecture was calculated to be 144.9 $m^2\ g^{-1}$, which is about 4.6-times that of pristine MoS_2 (31.5 $m^2\ g^{-1}$). This boosted surface area originates from the confined growth of MoS_2 and vertically aligned nanosheets, as shown in the SEM image of Fig. 1d. Moreover, the confined growth of MoS_2 indirectly results in the exposure of electroactive S–Mo–S edges [12]. This boosted surface area combined with more exposed electroactive S–Mo–S edges may contribute to the superior HER catalytic activity and enhanced supercapacitive performance.

Raman spectra were recorded to obtain structural information about the pristine MoS_2 and the h-rGO@MoS_2 architecture, as shown in Figs. 2c and S6. For pristine MoS_2, the two peaks located at 371 and 401 cm^{-1} are ascribed to the E^1_{2g} and A^1_g modes, respectively [42], and the frequency difference between the E^1_{2g} and A^1_g vibrational modes is about 30 cm^{-1}. Importantly, a redshift is observed after MoS_2 nanosheets had vertically grown on h-rGO, and the frequency difference between the E^1_{2g} and A^1_g vibration modes is reduced to 27 cm^{-1}, demonstrating reduced number of MoS_2 layers [40]. This agrees well with the results obtained from the TEM images (Figs. 1g and S2). In addition, the two weak peaks situated at 1350 and 1590 cm^{-1} correspond to the D and G peaks of h-rGO, respectively [17], further revealing the successful formation of h-rGO@MoS_2 composite with a trace amount of h-rGO.

To identify the chemical composition and surface electronic states of pristine MoS_2 and h-rGO@MoS_2, XPS measurements were carried out. The survey spectra of pristine MoS_2 and h-rGO@MoS_2 are shown in Fig. 2d and contain peaks corresponding to sulfur, molybdenum, carbon, and oxygen, and the calculated Mo/S atomic ratio is about 1/2, confirming the formation of MoS_2. As shown in Fig. S7, the C 1*s* peaks of pristine MoS_2 and h-rGO@MoS_2 can be deconvoluted into three peaks and assigned to the sp^2 hybrid C (C–C/C=C, 284.8 eV), hydroxyl C (C–O, 286.5 eV), and epoxy C (C=O, 288.5 eV), respectively [42]. It should be noted that the carbon in pristine MoS_2 is mainly derived from the carbon additive used during measurement. Importantly, for the C 1*s* peaks of h-rGO@MoS_2, the oxygen-containing groups yield low-intensity peaks, demonstrating that GO has been successfully reduced to rGO. The high-resolution Mo 3*d* spectrum of pristine MoS_2 (Fig. 2e) can be deconvoluted into two doublet peaks located at 232.8 and 229.4 eV and at 231.8 and 228.6 eV, assigned to Mo^{6+} and Mo^{4+}, respectively. In addition, the small peak at 235.5 eV probably originated from $(NH_4)_2MoS_4$ formed during the hydrothermal reaction. Concerning the Mo 3*d* spectrum of h-rGO@MoS_2, a single doublet peak situated at 233 and 229.8 eV can be attributed to Mo $3d_{3/2}$ and Mo $3d_{5/2}$, respectively, revealing the dominance of Mo^{4+} in MoS_2. Notably, a positive shift in the Mo 3d spectrum is observed when forming h-rGO@MoS_2, demonstrating the intense electron coupling effects between h-rGO and MoS_2 [17]. Likewise, the high-resolution S 2*p* spectra of pristine MoS_2 and h-rGO@MoS_2 were measured, as shown in Fig. 2f. Two peaks fitted to S $2p_{1/2}$ and $2p_{3/2}$ appeared in the spectra of both MoS_2 and h-rGO@MoS_2, verifying the existence of terminal S^{2-} ions, which are favorable for HER activity [43]. Moreover, the unexpected peak located at 164.3 eV in the spectrum of pristine MoS_2 is derived from $(NH_4)_2MoS_4$, as discussed above.

Linear sweep voltammetry (LSV) was carried out to understand the HER performance of h-rGO@MoS_2; bare

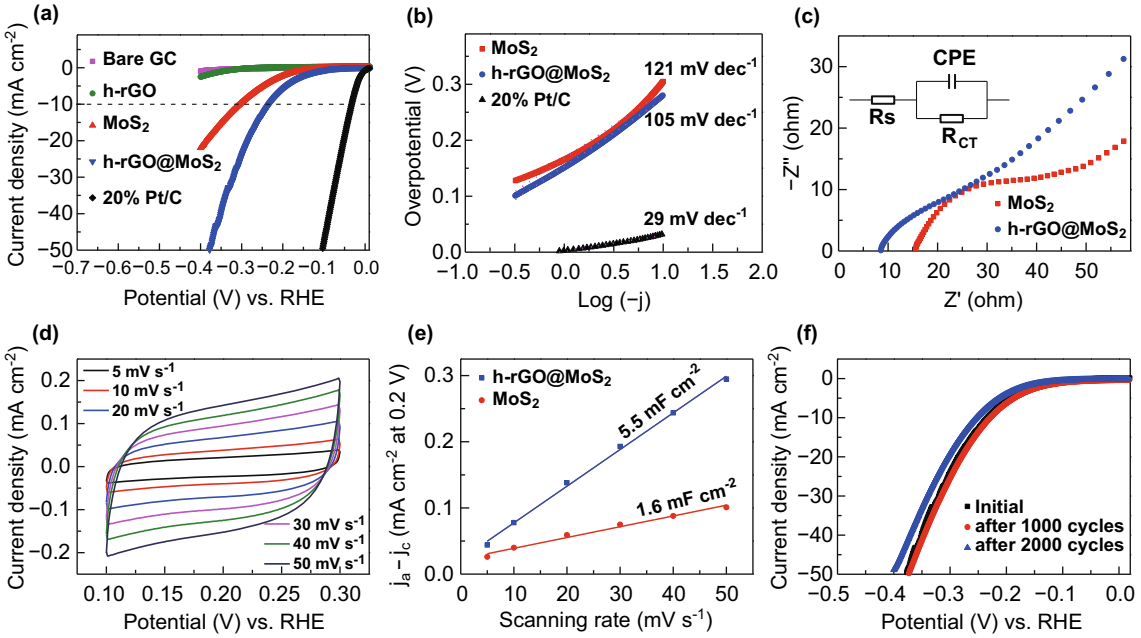

Fig. 3 **a** Polarization curves of bare GC, h-rGO, pristine MoS_2, h-rGO@MoS_2, and commercial 20% Pt/C in 0.5 M H_2SO_4 electrolyte at 5 mV s^{-1}, and **b** the corresponding Tafel plots of electrocatalysts in **a**. **c** EIS plots of pristine MoS_2 and h-rGO@MoS_2 from 10^{-2} to 10^5 Hz. **d** The electrochemical double-layer capacitances of h-rGO@MoS_2 ranging from 0.1 to 0.3 V at various scan rates (5, 10, 20, 30, 40, and 50 mV s^{-1}) in 0.5 M H_2SO_4. **e** The capacitive current at 0.20 V as a function of scan rate for pristine MoS_2 and h-rGO@MoS_2 in 0.5 M H_2SO_4 electrolyte. **f** Polarization curves of the h-rGO@MoS_2 electrocatalysts initially and after 1000 and 2000 cycles in 0.5 M H_2SO_4 electrolyte

GC, h-rGO, pristine MoS_2, and commercial Pt/C (20%) were also evaluated as a comparison. The corresponding polarization curves in Fig. 3a were obtained at a sweep rate of 5 mV s^{-1} in 0.5 M H_2SO_4 without *i*R compensation. Bare GC and h-rGO exhibit negligible HER performance, even at overpotential of 400 mV. In contrast, commercial Pt/C (20%) shows the best HER performance with near-zero onset overpotential. As for h-rGO@MoS_2, the onset potential is found at ca. 105 mV, which is much lower than that of pristine MoS_2 (− 162 mV). Further, the overpotential of h-rGO@MoS_2 at 10 mA cm^{-2} is about 230 mV, about 76 mV lower than that of pristine MoS_2 (306 mV). To elucidate the HER mechanism further, Tafel slopes are extracted from the linear portions of the Tafel plots (Fig. 3b). Commercial Pt/C (20%) exhibits a Tafel slope as low as 29 mV dec^{-1}, as previously reported [44]. For pristine MoS_2 and h-rGO@MoS_2, the Tafel slopes are calculated to be 121 and 105 mV dec^{-1}, respectively, demonstrating that the Volmer–Heyrovsky mechanism is the rate-limiting step [17]. The performance of the h-rGO@MoS_2 architecture is compared to those of other previously reported hollow MoS_2 microspheres or rGO/MoS_2 composites in Table S1. Because of the specific hollow architecture with vertically aligned MoS_2 nanosheets, the h-rGO@MoS_2 shows a superior onset overpotential.

EIS tests were carried out for both MoS_2 and h-rGO@MoS_2 to estimate the internal resistance properties. As shown by Fig. 3c, the charge transfer resistance of h-rGO@MoS_2 is about 15 Ω, which is smaller than its counterpart MoS_2 (28 Ω). This smaller internal resistance stems from the increased conductivity and shortened electron transfer pathways [33], which favor ion permeation and electron transfer, thus improving the HER catalytic performance. Besides the internal resistance, the electrochemical active surface area (ECSA) is another significant factor that has an impact on the HER performance. The corresponding electrochemical double-layer capacitances of h-rGO@MoS_2 and MoS_2 were measured by CV (ranging from 0.1 to 0.3 V) at different scan rates, as shown in Figs. 3d and S8. Moreover, a linear relationship between the scan rate and current density is observed, as shown in Fig. 3e. Based on the calculation, h-rGO@MoS_2 has a capacitance of 5.5 mF cm^{-2}, which is 3.5 times higher than that of pristine MoS_2. In other words, the electrochemically active sites are boosted after the vertical growth of MoS_2 on h-rGO, and this increase in electrochemically active sites no doubt enhanced the intrinsic HER activity of MoS_2. Additionally, long-term cycling tests of h-rGO@MoS_2 are examined by continuous cyclic voltammetry measurements between -0.4 and 0.1 V versus RHE at 50 mV s^{-1} in Fig. 3f. Clearly, negligible performance decay is observed after the first 1000 CV

cycles. Moreover, slight decay is seen after 2000 CV cycles, demonstrating the remarkable stability of h-rGO@MoS_2.

In this study, hollow rGO spheres were used as a matrix to confine the growth of MoS_2 and prevent its agglomeration. Note that the improved HER catalytic activity is derived from a synergistic effect, combining the following three aspects: (1) the expanded (002) interlayer spacing that increases the diffusion kinetics of ions and the intralayer conductivity [41]; (2) the ultrathin vertically aligned MoS_2 with a large number of exposed electroactive sites and increased contact area with the electrolyte [24]; and (3) the improved conductivity that accelerates electron transfer [45]. Thanks to the aforementioned synergistic effects, h-rGO@MoS_2 shows superior HER performance.

Further, the supercapacitive performance of h-rGO@MoS_2 was evaluated using CV and GCD measurements in 1 M Na_2SO_4 electrolyte. As shown in Fig. 4a, various applied scan rates (ranging from 5 to 200 mV s^{-1}) were selected to evaluate the rate performance of h-rGO@MoS_2. With increasing scan rate, the current densities gradually increased, and they remain almost near-rectangular at all tested scan rates, suggesting the high rate performance of h-rGO@MoS_2. The specific capacitance is calculated as $C_s = \int I dv / vm\Delta V$, where I (A), v (V s^{-1}), ΔV (V), and m (g) are the response current, scan rate, potential window, and the mass of active electrode material, respectively. According to the CV curves, the specific capacitances are found to be 146, 142, 138, 123, 112, and 90 F g^{-1} at scan rates of 5, 10, 20, 50, 100, and 200 mV s^{-1}, respectively. In the case of the pristine MoS_2 electrode, however, the shapes of the CV curves change from near-rectangular to twisted ellipses as the scan rate increased from 5 to 200 mV s^{-1}, revealing its less capacitive but more resistive performance (Fig. S9). To compare the capacitance and rate performance of MoS_2 and the h-rGO@MoS_2 architecture, the CV curves are compared at a sweep rate of 100 mV s^{-1} in Fig. S10. The CV curve of the h-rGO@MoS_2 architecture has a typical rectangular shape with a large area, while the shape of pristine MoS_2 has become a tilted ellipse.

Regarding the specific capacitance, h-rGO@MoS_2 shows a higher capacitance value (112 F g^{-1}) than that of pristine MoS_2 (30 F g^{-1}). This high capacitance and good rate performance arise from the formation of vertical 3D architectures, as shown in Fig. 1d, which allow electrolyte ions to access the interior surfaces of the electrode more easily and shorten the permeation distance, resulting in

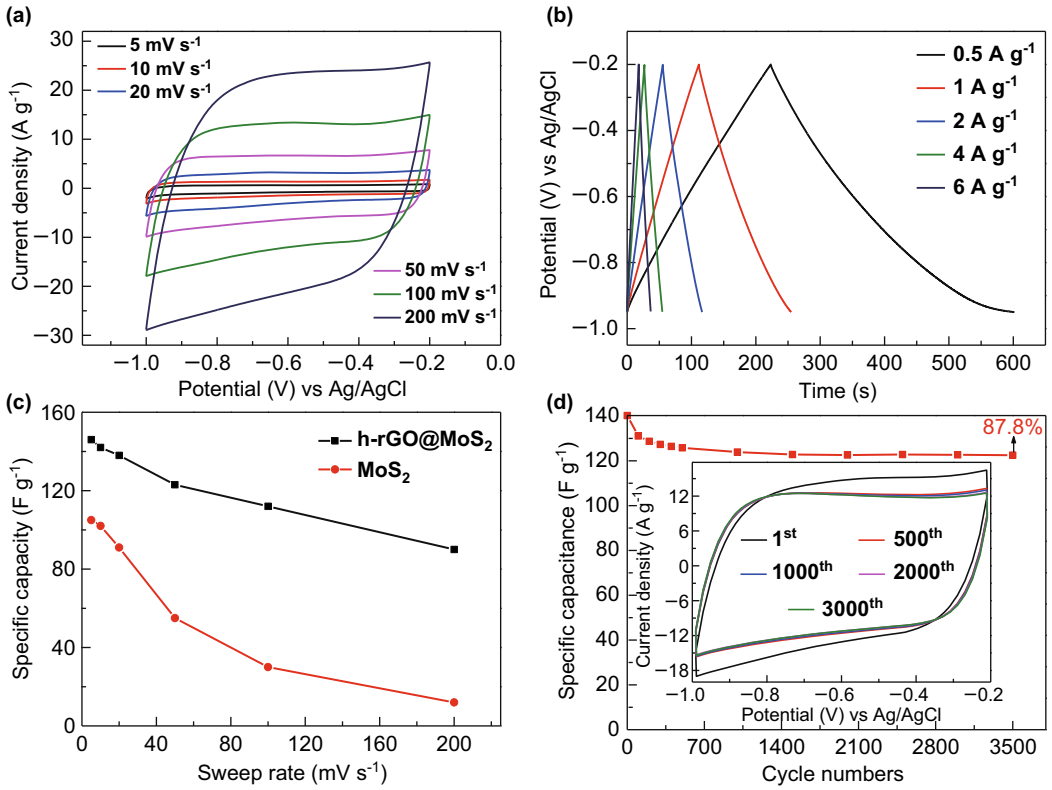

Fig. 4 **a** CV curves of h-rGO@MoS_2 electrode at various sweep rates (5, 10, 20, 50, 100, and 200 mV s^{-1}) in 1 M Na_2SO_4 electrolyte. **b** Galvanostatic curves of h-rGO@MoS_2 at various current densities (0.5, 1, 2, 4, and 6 A g^{-1}). **c** Capacitance retention property of h-rGO@MoS_2 and MoS_2 at sweep rates from 5 to 200 mV s^{-1}. **d** Cycle stability and capacitance retention of the h-rGO@MoS_2 electrode tested at a scan rate of 100 mV s^{-1}; the inset shows the CV curves for the 1st, 500th, 1000th, 2000th, and 3000th cycles

increased capacitive performance. Galvanostatic charge–discharge measurements were conducted at various current densities from 0.5 to 6 A g^{-1} in a potential window of − 1 to − 0.2 V. As shown in Fig. 4b, the charge curves are approximately linear and symmetric with their discharge counterparts, which further indicate the double electrode layer capacitance and excellent reversibility of the h-rGO@MoS_2 architecture [16]. The specific capacitances of the h-rGO@MoS_2 architecture are calculated using $C = I\Delta t/\Delta V$, where C is the specific capacitance, I is the constant discharge current density, Δt is the discharging time, and ΔV is the potential window. The specific capacitance of h-rGO@MoS_2 was calculated to be 238 F g^{-1} at a current density of 0.5 A g^{-1}.

Moreover, even at a high current density of 6 A g^{-1} the specific capacitance remained 135 F g^{-1}, which demonstrates the excellent rate performance. However, the specific capacitance of pristine MoS_2 can only reach 106 F g^{-1} at a current density of 0.5 A g^{-1}, and reduced to 41.2 F g^{-1} when the current density is increased to 6 A g^{-1} (Fig. S11). The supercapacitive performances of MoS_2/graphene-based materials are summarized and compared in Table S2. As shown, the h-rGO@MoS_2 architecture has a better specific capacitance than the other materials, which probably originates from the synergistic effect of the large surface area for the adsorption–desorption of ions and increased conductivity.

The capacitance during ultrafast charging/discharging was tested for pristine MoS_2 and h-rGO@MoS_2 (the results are shown in Fig. 4c). At a sweep rate of 5 mV s^{-1}, the specific capacitance of h-rGO@MoS_2 is ca. 146 F g^{-1}, which is ca. 1.4 times higher than that of pristine MoS_2 (105 F g^{-1}). As the sweep rate increased from 5 to 200 mV s^{-1}, the specific capacitance of the h-rGO@MoS_2 electrode decreased, but still achieved remarkable capacitance retention of 60% with a 40-fold increase in sweep rate. The specific capacitance of pristine MoS_2 decreased sharply with increasing sweep rate and only 10% capacitance is retained at sweep rate of 200 mV s^{-1}. The significant discrepancy in the rate capabilities of the h-rGO@MoS_2 electrode and pristine MoS_2 demonstrate that the introduction of graphene and the formation of vertical architectures contributed to boosting the capacitance retention performance.

The cycling stability is another significant factor that impacts the large-scale application of supercapacitors. The evaluation of the cycling stability of pristine MoS_2 and h-rGO@MoS_2 was investigated by CV cycling at a sweep rate of 100 mV s^{-1}. As shown in Fig. S12, pristine MoS_2 displayed stable cyclic behavior. With the 3D vertical architecture, the capacitance of the h-rGO@MoS_2 electrode showed an approximately 10% reduction in the first 400 cycles (Fig. 4d), which probably arises from the volume change of the active materials during the CV processes. In the subsequent 500–3500 cycles, the capacitance of h-rGO@MoS_2 remained steady at 87.7% of its initial capacitance, demonstrating the excellent long-term cycling stability.

4 Conclusions

In summary, 3D rGO hollow sphere-supported ultrathin MoS_2 nanosheets have been prepared, and show enhanced HER catalytic activity and supercapacitive performance compared to pristine MoS_2. The enhanced HER catalytic activity and supercapacitive performance are mainly derived from the following three factors: (1) the vertically aligned hierarchical architecture, which provides a large surface area for the adsorption, desorption, and diffusion of ions; (2) the relatively thin MoS_2 sheets, which provides more active sites and expanded interlayer spacing; and (3) the increased conductivity. Our strategy for constructing 3D architectures of vertically aligned nanosheets supported on hollow spheres may be applied to 3D composites of other materials and offers the potential for the development of efficient HER catalysts and advanced supercapacitor electrodes.

Acknowledgements This work is financially supported by the Natural Science Foundation of China (Grant No. 21473093), Fundamental Research Funds for the Central Universities and Tianjin Research Program of Application Foundation and Advanced Technology (Grant No. 14JCYBJC41300), and Ph.D. Candidate Research Innovation Fund of Nankai University. The authors thank Prof. Haijun Chen for using his BET facility.

Open Access This article is distributed under the terms of the Creative Commons Attribution 4.0 International License (http://creativecommons.org/licenses/by/4.0/), which permits unrestricted use, distribution, and reproduction in any medium, provided you give appropriate credit to the original author(s) and the source, provide a link to the Creative Commons license, and indicate if changes were made.

References

1. J. Zhang, T. Wang, P. Liu, Z. Liao, S. Liu, X. Zhuang, M. Chen, E. Zschech, X. Feng, Efficient hydrogen production on $MoNi_4$ electrocatalysts with fast water dissociation kinetics. Nat. Commun. **8**, 15437 (2017). https://doi.org/10.1038/ncomms15437
2. Y.Y. Chen, Y. Zhang, X. Zhang, T. Tang, H. Luo, S. Niu, Z.H. Dai, L.J. Wan, J.S. Hu, Self-templated fabrication of $MoNi_4$/MoO_{3-x} nanorod arrays with dual active components for highly efficient hydrogen evolution. Adv. Mater. **29**(39), 1703311 (2017). https://doi.org/10.1002/adma.201703311
3. M. Kuang, Q. Wang, P. Han, G. Zheng, Cu, Co-embedded N-enriched mesoporous carbon for efficient oxygen reduction and hydrogen evolution reactions. Adv. Energy Mater. (2017). https://doi.org/10.1002/aenm.201700193

4. M. Acerce, D. Voiry, M. Chhowalla, Metallic 1T phase MoS_2 nanosheets as supercapacitor electrode materials. Nat. Nanotechnol. **10**(4), 313–318 (2015). https://doi.org/10.1038/nnano.2015.40
5. X. Li, X. Li, J. Cheng, D. Yuan, W. Ni, Q. Guan, L. Gao, B. Wang, Fiber-shaped solid-state supercapacitors based on molybdenum disulfide nanosheets for a self-powered photodetecting system. Nano Energy **21**, 228–237 (2016). https://doi.org/10.1016/j.nanoen.2016.01.011
6. K. Peng, L. Fu, J. Ouyang, H. Yang, Emerging parallel dual 2D composites: natural clay mineral hybridizing MoS_2 and interfacial structure. Adv. Funct. Mater. **26**(16), 2666–2675 (2016). https://doi.org/10.1002/adfm.201504942
7. M.A. Lukowski, A.S. Daniel, F. Meng, A. Forticaux, L. Li, S. Jin, Enhanced hydrogen evolution catalysis from chemically exfoliated metallic MoS_2 nanosheets. J. Am. Chem. Soc. **135**(28), 10274–10277 (2013). https://doi.org/10.1021/ja404523s
8. X. Hai, W. Zhou, S. Wang, H. Pang, K. Chang, F. Ichihara, J. Ye, Rational design of freestanding MoS_2 monolayers for hydrogen evolution reaction. Nano Energy **39**, 409–417 (2017). https://doi.org/10.1016/j.nanoen.2017.07.021
9. Z. Wu, B. Fang, Z. Wang, C. Wang, Z. Liu et al., MoS_2 nanosheets: a designed structure with high active site density for the hydrogen evolution reaction. ACS Catal. **3**(9), 2101–2107 (2013). https://doi.org/10.1021/cs400384h
10. J. Guo, C. Liu, Y. Sun, J. Sun, W. Zhang, T. Si, H. Lei, Q. Liu, X. Zhang, N-doped MoS_2 nanosheets with exposed edges realizing robust electrochemical hydrogen evolution. J. Solid State Chem. **263**, 84–87 (2018). https://doi.org/10.1016/j.jssc.2018.04.023
11. X. Zhang, Y. Wu, Y. Sun, P. Ding, Q. Liu, L. Tang, J. Guo, Hybrid of $Fe_4[Fe(CN)_6]_3$ nanocubes and MoS_2 nanosheets on nitrogen-doped graphene realizing improved electrochemical hydrogen production. Electrochim. Acta **263**, 140–146 (2018). https://doi.org/10.1016/j.electacta.2018.01.051
12. Y. Kim, D.H.K. Jackson, D. Lee, M. Choi, T.W. Kim et al., In situ electrochemical activation of atomic layer deposition coated MoS_2 basal planes for efficient hydrogen evolution reaction. Adv. Funct. Mater. **27**(34), 1701825 (2017). https://doi.org/10.1002/adfm.201701825
13. B. Guo, K. Yu, H. Li, H. Song, Y. Zhang, X. Lei, H. Fu, Y. Tan, Z. Zhu, Hollow structured micro/nano MoS_2 spheres for high electrocatalytic activity hydrogen evolution reaction. ACS Appl. Mater. Interfaces **8**(8), 5517–5525 (2016). https://doi.org/10.1021/acsami.5b10252
14. J. Guo, X. Zhang, Y. Sun, L. Tang, X. Zhang, $NiMoS_3$ nanorods as PH-tolerant electrocatalyst for efficient hydrogen evolution. ACS Sustain. Chem. Eng. **5**(10), 9006–9013 (2017). https://doi.org/10.1021/acssuschemeng.7b01802
15. X. Li, C. Zhang, S. Xin, Z. Yang, Y. Li, D. Zhang, P. Yao, Facile synthesis of MoS_2/reduced graphene oxide@polyaniline for high-performance supercapacitors. ACS Appl. Mater. Interfaces **8**(33), 21373–21380 (2016). https://doi.org/10.1021/acsami.6b06762
16. E.G. da Silveira Firmiano, A.C. Rabelo, C.J. Dalmaschio, A.N. Pinheiro, E.C. Pereira, W.H. Schreiner, E.R. Leite, Supercapacitor electrodes obtained by directly bonding 2D MoS_2 on reduced graphene oxide. Adv. Energy Mater. **4**(6), 1301380 (2014). https://doi.org/10.1002/aenm.201301380
17. Y. Li, H. Wang, L. Xie, Y. Liang, G. Hong, H. Dai, MoS_2 nanoparticles grown on graphene: an advanced catalyst for the hydrogen evolution reaction. J. Am. Chem. Soc. **133**(19), 7296–7299 (2011). https://doi.org/10.1021/ja201269b
18. M. Yu, S. Zhao, H. Feng, L. Hu, X. Zhang, Y. Zeng, Y. Tong, X. Lu, Engineering thin MoS_2 nanosheets on TiN nanorods: advanced electrochemical capacitor electrode and hydrogen evolution electrocatalyst. ACS Energy Lett. **2**(8), 1862–1868 (2017). https://doi.org/10.1021/acsenergylett.7b00602
19. J. Cao, J. Zhou, Y. Zhang, X. Liu, A clean and facile synthesis strategy of MoS_2 nanosheets grown on multi-wall CNTs for enhanced hydrogen evolution reaction performance. Sci. Rep. **7**(1), 8825 (2017). https://doi.org/10.1038/s41598-017-09047-x
20. L. Yang, W. Zhou, J. Lu, D. Hou, Y. Ke, G. Li, Z. Tang, X. Kang, S. Chen, Hierarchical spheres constructed by defect-rich MoS_2/-carbon nanosheets for efficient electrocatalytic hydrogen evolution. Nano Energy **22**, 490–498 (2016). https://doi.org/10.1016/j.nanoen.2016.02.056
21. W. Zhou, K. Zhou, D. Hou, X. Liu, G. Li, Y. Sang, H. Liu, L. Li, S. Chen, Three-dimensional hierarchical frameworks based on MoS_2 nanosheets self-assembled on graphene oxide for efficient electrocatalytic hydrogen evolution. ACS Appl. Mater. Interfaces **6**(23), 21534–21540 (2014). https://doi.org/10.1021/am506545g
22. Y. Liu, Y. Zhu, X. Fan, S. Wang, Y. Li, F. Zhang, G. Zhang, W. Peng, (0D/3D) MoS_2 on porous graphene as catalysts for enhanced electrochemical hydrogen evolution. Carbon **121**, 163–169 (2017). https://doi.org/10.1016/j.carbon.2017.05.092
23. C. Tang, L. Zhong, B. Zhang, H.F. Wang, Q. Zhang, 3D mesoporous van der Waals heterostructures for trifunctional energy electrocatalysis. Adv. Mater. **30**(5), 1705110 (2017). https://doi.org/10.1002/adma.201705110
24. G. Wang, J. Zhang, S. Yang, F. Wang, X. Zhuang, K. Müllen, X. Feng, Vertically aligned MoS_2 nanosheets patterned on electrochemically exfoliated graphene for high-performance lithium and sodium storage. Adv. Energy Mater. **8**(8), 1702254 (2017). https://doi.org/10.1002/aenm.201702254
25. Q. Yun, Q. Lu, X. Zhang, C. Tan, H. Zhang, Three-dimensional architectures constructed from transition-metal dichalcogenide nanomaterials for electrochemical energy storage and conversion. Angew. Chem. Int. Edit. **57**(3), 626–646 (2018). https://doi.org/10.1002/anie.201706426
26. Q. Wang, K. Rui, C. Zhang, Z. Ma, J. Xu, W. Sun, W. Zhang, J. Zhu, W. Huang, Interlayer-expanded metal sulfides on graphene triggered by a molecularly self-promoting process for enhanced lithium ion storage. ACS Appl. Mater. Interfaces **9**(46), 40317–40323 (2017). https://doi.org/10.1021/acsami.7b13763
27. L. Sheng, T. Wei, Y. Liang, L. Jiang, L. Qu, Z. Fan, Vertically oriented graphene nanoribbon fibers for high-volumetric energy density all-solid-state asymmetric supercapacitors. Small **13**(22), 1700371 (2017). https://doi.org/10.1002/smll.201700371
28. X. Yang, Z. Zhang, Y. Fu, Q. Li, Porous hollow carbon spheres decorated with molybdenum diselenide nanosheets as anodes for highly reversible lithium and sodium storage. Nanoscale **7**(22), 10198–10203 (2015). https://doi.org/10.1039/c5nr01909e
29. Y. Wang, Z. Chen, T. Lei, Y. Ai, Z. Peng et al., Hollow $NiCo_2S_4$ nanospheres hybridized with 3D hierarchical porous rGO/Fe_2O_3 composites toward high-performance energy storage device. Adv. Energy Mater. **8**(16), 1703453 (2018). https://doi.org/10.1002/aenm.201703453
30. X. Zhang, Y.P. Zhou, B. Luo, H.C. Zhu, W. Chu, K.M. Huang, Microwave-assisted synthesis of $NiCo_2O_4$ double-shelled hollow spheres for high-performance sodium ion batteries. Nano-Micro Lett. **10**(1), 13 (2017). https://doi.org/10.1007/s40820-017-0164-2
31. R. Xing, T. Zhou, Y. Zhou, R. Ma, Q. Liu, J. Luo, J. Wang, Creation of triple hierarchical micro-meso-macroporous N-doped carbon shells with hollow cores toward the electrocatalytic oxygen reduction reaction. Nano-Micro Lett. **10**(1), 3 (2017). https://doi.org/10.1007/s40820-017-0157-1
32. T.W. Lin, H.C. Tsai, T.Y. Chen, L.D. Shao, Facile and controllable one-pot synthesis of hierarchical Co_9S_8 hollow microspheres as high-performance electroactive materials for energy storage and conversion. ChemElectroChem **5**(1), 137–143 (2018). https://doi.org/10.1002/celc.201700886

33. Z. Li, A. Ottmann, T. Zhang, Q. Sun, H.P. Meyer, Y. Vaynzof, J. Xiang, R. Klingeler, Preparation of hierarchical C@MoS_2@C sandwiched hollow spheres for lithium ion batteries. J. Mater. Chem. A **5**(8), 3987–3994 (2017). https://doi.org/10.1039/c6ta10439h
34. L. Yu, H. Hu, H.B. Wu, X.W. Lou, Complex hollow nanostructures: synthesis and energy-related applications. Adv. Mater. **29**(15), 1604563 (2017). https://doi.org/10.1002/adma.201604563
35. C. Hu, S. Zheng, C. Lian, Q. Hu, S. Duo, R. Zhang, F. Chen, CTAB-assisted synthesis of S@rGO composite with enhanced photocatalytic activity and photostability. Appl. Surf. Sci. **335**, 92–98 (2015). https://doi.org/10.1016/j.apsusc.2015.02.031
36. M. Wang, J. Han, H. Xiong, R. Guo, Y. Yin, Nanostructured hybrid shells of r-GO/AuNP/m-TiO_2 as highly active photocatalysts. ACS Appl. Mater. Interfaces **7**(12), 6909–6918 (2015). https://doi.org/10.1021/acsami.5b00663
37. M. Wang, J. Han, H. Xiong, R. Guo, Yolk@shell Nanoarchitecture of Au@r-GO/TiO_2 hybrids as powerful visible light photocatalysts. Langmuir **31**(22), 6220–6228 (2015). https://doi.org/10.1021/acs.langmuir.5b01099
38. B. Xie, Y. Chen, M. Yu, T. Sun, L. Lu, T. Xie, Y. Zhang, Y. Wu, Hydrothermal synthesis of layered molybdenum sulfide/N-doped graphene hybrid with enhanced supercapacitor performance. Carbon **99**, 35–42 (2016). https://doi.org/10.1016/j.carbon.2015.11.077
39. H. Ji, C. Liu, T. Wang, J. Chen, Z. Mao, J. Zhao, W. Hou, G. Yang, Porous hybrid composites of few-layer MoS_2 nanosheets embedded in a carbon matrix with an excellent supercapacitor electrode performance. Small **11**(48), 6480–6490 (2015). https://doi.org/10.1002/smll.201502355
40. X. Zhang, R. Zhao, Q. Wu, W. Li, C. Shen, L. Ni, H. Yan, G. Diao, M. Chen, Petal-like MoS_2 nanosheets space-confined in hollow mesoporous carbon spheres for enhanced lithium storage performance. ACS Nano **11**(8), 8429–8436 (2017). https://doi.org/10.1021/acsnano.7b04078
41. K.D. Rasamani, F. Alimohammadi, Y. Sun, Interlayer-expanded MoS_2. Mater. Today **20**(2), 83–91 (2017). https://doi.org/10.1016/j.mattod.2016.10.004
42. C. Zhao, C. Yu, M. Zhang, H. Huang, S. Li et al., Ultrafine MoO_2-carbon microstructures enable ultralong-life power-type sodium ion storage by enhanced pseudocapacitance. Adv. Energy Mater. **7**(15), 1602880 (2017). https://doi.org/10.1002/aenm.201602880
43. H. Vrubel, D. Merki, X. Hu, Hydrogen evolution catalyzed by MoS_3 and MoS_2 particles. Energy Environ. Sci. **5**(3), 6136–6144 (2012). https://doi.org/10.1039/c2ee02835b
44. F. Yang, Y. Chen, G. Cheng, S. Chen, W. Luo, Ultrathin nitrogen-doped carbon coated with CoP for efficient hydrogen evolution. ACS Catal. **7**(6), 3824–3831 (2017). https://doi.org/10.1021/acscatal.7b00587
45. W. Zhou, D. Hou, Y. Sang, S. Yao, J. Zhou, G. Li, L. Li, H. Liu, S. Chen, MoO_2 nanobelts@nitrogen self-doped MoS_2 nanosheets as effective electrocatalysts for hydrogen evolution reaction. J. Mater. Chem. A **2**(29), 11358–11364 (2014). https://doi.org/10.1039/c4ta01898b